

Enhancing Worldwide Image Geolocation by Ensembling Satellite-Based Ground-Level Attribute Predictors

Michael J. Bianco

mike.bianco@clarifai.com

David Eigen

deigen@clarifai.com

Michael Gormish

michael.gormish@clarifai.com

Clarifai Inc., San Francisco

Abstract

Geolocating an image of a ground-level scene entails estimating the location on Earth where the picture was taken, in absence of GPS or other location metadata. Typically, methods are evaluated by measuring the Great Circle Distance (GCD) between a predicted location and the ground truth. However, this measurement is limited because it only evaluates a single point, not estimates of regions or score heatmaps. This is especially important in applications to rural, wilderness and under-sampled areas, where finding the exact location may not be possible, and when used in aggregate systems that progressively narrow down locations.

In this paper, we introduce a novel metric, Recall vs Area (RvA), which measures the accuracy of estimated distributions of locations. RvA treats image geolocation results similarly to document retrieval, measuring recall as a function of area: For a ranked list of (possibly non-contiguous) predicted regions, we measure the accumulated area required for the region to contain the ground truth coordinate. This produces a curve similar to a precision-recall curve, where “precision” is replaced by square kilometers area, allowing evaluation of performance for different downstream search area budgets.

Following directly from this view of the problem, we then examine a simple ensembling approach to global-scale image geolocation, which incorporates information from multiple sources to help address domain shift, and can readily incorporate multiple models, attribute predictors, and data sources. We study its effectiveness by combining the geolocation models GeoEstimation [12] and the current SOTA GeoCLIP [2], with attribute predictors based on LandScan [17] and ESA-CCI Land Cover [1]. We find significant improvements in image geolocation for areas that are under-represented in the training set, particularly non-urban areas, on both Im2GPS3k and Street View images.

1. Introduction

Accurate localization of ground-level imagery is of great significance to a variety of tasks, including navigation, tourism, and security, and the subject of recent research activity [2,4,6,12,21]. However, even large publicly available geotagged image datasets, such as MP-16 [9] and Street View [11], sample only a small fraction of the Earth’s surface and mostly concentrate on cities and other population centers. Moreover, much imagery that is available with labeled geographic coordinates is clustered around highly trafficked areas, such as famous landmarks, parks, restaurants and other sites of interest. These include most common benchmark datasets, e.g. Im2GPS3k [19] and YFCC26k [12,18]. Thus domain shift is a major problem as the imagery in many deployment applications do not reflect the training distribution, particularly when applied to rural areas or wilderness, or areas that are under-represented by the datasets’ collection methods.

We introduce a novel image geolocation metric, *Recall vs Area (RvA)*. This metric helps account for ground-level image similarity from different geographic regions, and naturally characterizes model performance when predicted regions are discontinuous. It is particularly apt for measuring systems that suggest areas for downstream tasks, for example, to be further refined using landmark-matching or other more expensive methods, or to flag images that may have come from certain regions of the globe for further study by human analysts. Further, the metric naturally enables ensembling geolocation models with additional ground-level attribute models.

To help address the challenge of generalization to under-sampled areas, we propose a general ensembling approach to global-scale image geolocation, which incorporates ground-level attribute predictors based on satellite data products. While ground level training data are generally limited, satellite datasets have global coverage. These predictors bring additional information to bear on the geolocation problem, e.g. relating global land cover types to available ground-level imagery. The attributes are assumed

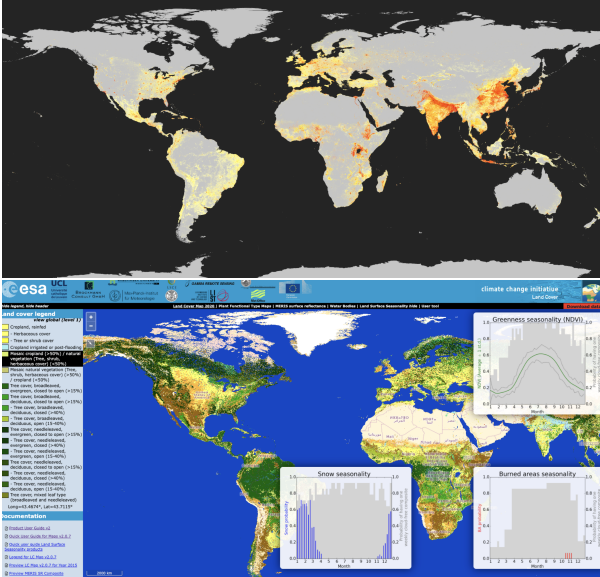


Figure 1. (TOP) LandScan global-scale population density [17], map from 2021. Higher population density indicated by warmer colors. (BOTTOM) ESA CCI Land Cover, online viewer [1].

proxy for geographically specific image scene concepts and objects. Estimates from these predictors are combined with those from other global geolocation models, e.g. GeoCLIP [2]. In addition, while most geolocation models require geotagged ground level imagery for training, many attribute predictors (e.g. vegetation, buildings, roads, etc.) can also leverage additional non-geotagged data sources in their training process.

We evaluate our method, combining the foundational GeoEstimation [12] and the recent SOTA GeoCLIP [2] approach with ground-level attributes corresponding to population density [17] and land use/land cover [1] maps, to demonstrate the utility of the additional features and validate our approach. In future work we plan on incorporating additional additional data sources and maps, such as OpenStreetMap tags.

We evaluate our models using both the standard Im2GPS3k [19], as well as a geo-diverse Street View dataset (see Sec. 4.2) that is different in geographic distribution and scene concepts from MP-16 and related benchmarks, as shown in Fig. 2. The Street View dataset was constructed by gathering at least 426 panoramas from 90 countries [11]. None of the Street View data was used in training our models, so it provides a reasonable measure of domain shift robustness.

1.1. Contributions

- We develop a novel metric, Recall vs Area, for evaluating geolocation systems, which can account for visual similarity of ground-level imagery across the Earth.



Figure 2. Batches of images from (left) MP-16 and (right) Street View, from medium urban density regions per LandScan labeling (see Sec. 4.2, 5.1). In general, the MP-16 dataset consists of more typical urban scenes, whereas Street View contains more scenery from near roads. Further MP-16 dataset is drawn from areas much more close to urban environments.

We use this method to assess image geolocation approaches.

- We show that, in isolation, geolocation methods trained only on geotagged imagery can be vulnerable to image domain shift with respect to training data.
- We develop an approach to combine ground-level attribute predictors, based on satellite data products, with geolocation models. The incorporation of ground-level information related to satellite data promises to improve generalization to areas of the Earth for which there are few ground-level picture samples.
- We show ensembling ground-level attribute predictors improves image geolocation performance on both in- and out-of-domain datasets on SOTA image geolocation methods.

2. Related Work

Müller-Budack et al. [12] develop a hierarchical pixel-based approach to geolocation. They fine-tune their model on the large MP-16 dataset, and quantize the Earth using S^2 cells (using the Google S^2 geometry Library¹), with 3 resolutions {‘coarse’, ‘medium’, ‘fine’} depending on data density. The output of the model is image geolocations for each level. Subsequent papers have built on this work, proposing various ground-level gridding strategies, including CPLaNet [16] and Translocator [13].

Other recent works have brought additional information to the geolocation problem, including relationships between scene and geographic scales and variations in environment [4] and segmentation models [13]. In Luo et

¹<https://code.google.com/archive/p/s2-geometry-library/>

al. [11] and Cepeda et al. [2], geographical correlations encoded in vision-language foundation models (using Contrastive Language-Image Pretraining [14]) are exploited to improve image geolocation performance.

There is also significant work in cross-view image localization, e.g. [7, 10, 20]. In these approaches, optical satellite imagery is matched to ground level imagery to achieve ground level image localization. Generally, such methods are used to pinpoint exact locations within limited-area urban scenes where dense ground-level imagery is available. This is complementary to our work, which uses ground-level attributes estimated from satellite sources to limit search areas — indeed, these are examples of systems that might run downstream of ours.

Lin et al. [10] explored using land-cover information for improving query-based geolocation. Their approach required associated triples of ground-level and aerial imagery and land use, and apply their system to a small 40×40 km region. In a similar vein, we use land cover, along with other data sources, to improve geolocation performance globally.

As far as we are our aware, the approach we present is the first to use land cover and other attributes recognizable from ground level for global-scale geolocation. We further propose a novel approach for utilizing these features, in terms of ensembling the predictors with ‘strong’ geolocation models. Using a common prediction map, the predictions for each attribute mask are combined. This yields an effective intersection of the high confidence attributes, and has the potential to reduce image geolocation search area.

3. Approach

3.1. Recall vs Area Metric

The most common metric currently used to measure geolocation performance calculates the distance between a single predicted location and the ground truth coordinates. Localization accuracy is calculated for different distance radius buckets, measured using great circle distance (GCD). For example [12] used GCD thresholds of [1, 25, 200, 750, 2500] km to evaluate model performance, even giving these distances names to represent how close the solution was, namely street, city, region, country, continent.

While this measure works well to characterize performance of a single predicted location, it does not extend to measuring performance of a larger (possibly discontinuous) predicted area. This is important for many practical applications, where the image geolocation algorithm is used to propose a set of possible locations that are used in downstream tasks. Thus localization performance is measured in terms of an area budget.

In addition, many distant regions on Earth look similar from ground-level, as illustrated by the often scattered

global distribution of high confidence S^2 cell predictions by GeoEstimation. In the context of a system that progressively narrows down the possible locations an image was taken from, for example, it is important to maintain recall at each stage while still reducing the set of predicted regions.

We propose a new metric, *Recall vs Area*, to characterize image geolocation model performance. We rely on the conventions of recall and precision, and formulate a geographic analogy to document retrieval. For each image a set of region proposal areas can be obtained, sorted by confidence score. We then accumulate areas by score, up to a given search budget. Recall is determined according to whether the ground truth lies in this area. We then compute recall for different area budgets (thresholds), resulting in a ROC-like curve comparing recall on one axis and area budgets on the other.

Here, recall is determined by whether the geographic area returned by the model for a query image contains the image’s location. More formally, for a query image $x_i \in \mathcal{X}$ with ground truth location y_i , a geolocation model will return a list of location areas (S^2 cells, points, etc.) $a_{ik}, k \in [1..K]$, along with confidence scores. We accumulate area sorted by model confidence, to create a (possibly discontinuous) region, up to an area budget (threshold). For an area threshold α , recall is then

$$recall(\alpha) = \frac{\sum_i \mathbb{1}[y_i \in \{a_{ik} : \sum_{k'=1}^k a_{ik'} \leq \alpha\}]}{|\mathcal{X}|}, \quad (1)$$

i.e. the fraction of images whose ground-truth location lies within the model’s top-scoring predicted areas, up to the area threshold α .

We then plot the curve $recall(\alpha)$ for different values of the area budget α , resulting in a description of model performance, akin to a precision-recall curve (see Fig ??).² The curve is used to evaluate model performance, or to help select an appropriate trade-off between maintaining recall and size of a proposed area.

3.2. Algorithm

Given an image x , with corresponding geotag coordinates y , we ensemble geolocation and ground-level attribute predictors to find the a set of areas on Earth most likely to contain the image.

Because we combine the geolocation area predictions of multiple models, we map each of their outputs to a common image over the surface of the Earth, with “pixel” coordinates given by latitude and longitude (WGS-84 projection). Note that we index by (lat, lon), so each “pixel” has a different area on the Earth depending on its latitude coordinate. To account for this, we also create an array A_{pix} that

²Indeed, area itself can be thought of as a notion of inverse precision, with smaller areas being more precise and larger ones including more false positive locations and therefore less precise.

Algorithm 1 Rasterized GeoEstimation/GeoCLIP

Given $x, f, \mathcal{M}_f, \epsilon_p$
 $p = f(x)$ # S^2 cell probabilities and masks
 # sort probs and masks descending by probability
 $order = \text{argsort}(p)$
 $p = p[order]$
 $m = \mathcal{M}_f[order]$
 # combine into rasterized grid
 $P = \sum_{j=1} p_j m_j$
return P

Algorithm 2 Ensembling ground-level attribute predictors with Rasterized GeoEst., Algo. 1

Given $x, \{f_1 \dots f_K\}, \{\mathcal{M}_1 \dots \mathcal{M}_K\}$
return $P = \prod_{k=1}^K P_k$, with $P_k = \sum_j p_{kj} m_{kj}$ as in Alg.1

contains the surface area corresponding to each point in the map.

The output of each model $f(\cdot)$ is a vector of probabilities $p = [p_1 \dots p_J] \in \mathbb{R}^J$, corresponding a set of binary masks $\mathcal{M}_f = \{m_1 \dots m_J\}$, with $|\mathcal{M}| = J$, and $m \in \{0, 1\}^{H \times W}$ with H and W the vertical (latitude) and horizontal (longitude) resolution of the entire map. For LandScan and Land-Cover, each mask m_j is a discontinuous region corresponding to a population density bucket, land use type, etc. The output of each model is a map of probabilities over a “pixel” grid of latitude \times longitude.

For our analysis, we require rasterized versions of GeoEstimation [12] and GeoCLIP [2]. Because both are fine-tuned with MP-16, we use the S^2 cell centers, which are also distributed according to MP-16, to sample the GeoCLIP location encoder and obtain scores for each of the S^2 cells. We then assign the score of the center over the grid-sampled locations in each cell, normalized by area. With the output of the two methods in the same format, the same algorithm is used to rasterize the S^2 probabilities, shown in Algorithm 1. Each mask m_j corresponds to a single S^2 cell rasterized to the common image.

Image locations are estimated by probabilistically ensembling [3] the ground-level attribute predictors and geolocation estimator. In this work we use a simple element-wise product of probability maps to find the final prediction, which we found to be effective even though the masks are not independent:

$$P_{En.s.} = \prod_k P_k(x) \quad (2)$$

where each $P_k(x)$ is the probability map of the k^{th} predictor (GeoEst, Land Cover regions, etc.) as described in Algorithms 1 and 2. Since the approach assigns a score to each pixel in the common image, the model scores for each

Algorithm 3 Model evaluation

Given dataset \mathcal{D} , model, pixel spherical areas map A_{pix}
 Returns accumulated areas necessary to the include ground truth location for each image.
 $\mathcal{A} \leftarrow \{\}$ # eval. areas
for (image x_i , g.t.location y_i) $\in \mathcal{D}$ **do**
 $P \leftarrow \text{model}(x)$
 $p^* = P[y_i]$ # pred probability at ground truth location
 $area = \sum A_{pix} \cdot \mathbb{1}[P \geq p^*]$ # sum area of preds $\geq p^*$
 $\mathcal{A} \leftarrow \mathcal{A} \cup area$
end for
return \mathcal{A}

attribute mask are normalized by the corresponding mask area to produce a probability over pixels.

For evaluation, probabilities and mask areas are accumulated in score order for each image until the area contains the ground truth location. This gives us an array of the smallest cumulative area needed to contain the ground truth for each image — i.e. the smallest area threshold α at which each image prediction is a “hit”. This process is defined in Algorithm 3. We then sort this array to produce the Recall vs Area curve. In deployment, the area threshold can be used to calibrate the ensembled predictions to a desired level of recall, or recall to an area budget.

4. Datasets

4.1. Ground-level attribute datasets and processing

Here, we describe the satellite data products used to develop our Earth surface attribute models, and the image datasets we used to train and evaluate our ensembling approach and related methods.

In our processing, we consider two satellite data products: LandScan Global [17] from Oak Ridge National Laboratory (ORNL) and Land Cover [1], from the European Space Agency (ESA) Climate Change Initiative (CCI). Each data product provides high resolution estimates of surface attributes: LandScan Global predicts 24-hour average population density and ESA-CCI Land Cover predicts 38 natural and anthropogenic land cover classes.

We used three image datasets. MP-16 [18] and Im2GPS3k [19] are common training evaluation benchmarks in image geolocation literature. MP-16 was used to train our attribute classifiers, and Im2GPS3k was used for testing. Additionally, we collected a set of images from Google Street View, using training-set panorama IDs from [11] to evaluate the generalization of the models to image location distributions and image capture pipelines that do not match those of MP-16 and Im2GPS3k.

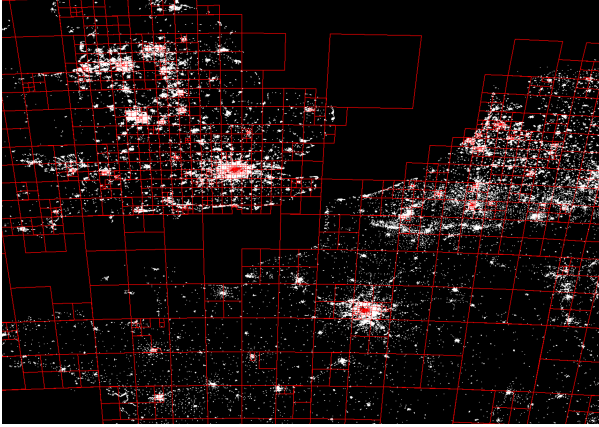


Figure 3. Example overlay centered on Europe, showing S^2 cells (red boxes, fine level from GeoEstimation [12]) with LandScan [17] medium population density mask (white). The mask is much more restrictive than the S^2 cells alone, yielding improvements in Recall vs Area from model ensembling.

4.1.1 LandScan Global

The ORNL LandScan Global dataset is a global map of population density at $\sim 1 \text{ km}^2$ resolution [17], see Fig. 1. The data is a large TIFF image, 21600×43200 pixels (lat x lon), with 24-hour average population densities.

Each pixel indicates whether the corresponding region is land and if so, the population density. The coordinate system of the image is WGS-84, which is a standard lat-long. representation. The resolution is $\sim 1 \text{ km}^2$.

4.1.2 ESA Landcover

ESA-CCI Land Cover is a global land cover and land use data product [1], see Fig. 1. It is generated using deep learning classifiers on Sentinel-2 satellite images. The product is a 64800×129600 pixel (lat x lon, WGS-84) GeoTIFF with 300 m resolution. Each pixel is labeled as the most likely land cover from 38 classes (22 super-classes), see Fig. 1. The classes include cropland, grassland, tree cover, and developed cover/use categories. Maps are available for the years 1992-2020. We used the ESA-CCA Land Cover 2015 dataset for development of region reduction classifiers.

4.2. Image datasets

Currently, the most comprehensive geotagged ground-level image dataset is MP-16 [9]. This dataset is a subset of the Yahoo Flickr Creative Commons 100 Million datasets (YFCC100M) [18], which have geotags. This dataset was used to train ground-level attribute predictors.

The size of the dataset is 4.7M images. We were able to obtain ~ 4.2 M of the total, as approximately 500 k were no longer available at the URLs provided by [12]. The MP-

16 image concepts and objects are quite diverse, with indoor and outdoor imagery of natural and human-made scenes and objects.

MP-16 was the training set from the GeoEstimation paper [12], and is still used today, e.g. [2, 13]. Im2GPS3k is an additional benchmark introduced in [19]. We use this dataset to test our models.

For evaluation, we use Im2GPS3k [19] and a collection of images from Google Street View [5]. To evaluate model generalization and specifically, the ‘domain-gap’ robustness of geolocation methods, we do not train on any of the Street View images, using them only for evaluation.

The Street View [5] data was obtained using the Google Street View panorama IDs from Luo et al [11]. The geodiverse Street View dataset was constructed by gathering at least 426 panoramas from 90 countries. From this overall distribution, train, valid and test sets were randomly constructed. We obtained the imagery using a subset of their training panorama IDs, chosen sequentially from the total of 322536 panoramas. Of the 50000 IDs chosen, 49829 IDs were still valid. We thus obtained 49829 images - each a single 90° FOV slice from a full panorama, with 15° downward pitch (toward ground for imaging road markings) from the Street View API and the corresponding image geotags.

5. Experiments

5.1. Ground-level attribute predictors

We trained two ground-level attribute predictors, one for each satellite data product (LandScan and Land Cover), using MP-16 imagery relabeled with attributes from each source. In our experiments, we use the acronyms LS for LandScan and LC for Land Cover. For each image, the ground-level attribute labels were obtained by indexing the nearest pixel value in the attribute maps at the native TIFF resolution. As described in Section 3.2 the outputs of these models are projected on global masks and combined to find a global distribution of probable locations.

Since the LS population densities are continuous, we mapped these to four density buckets for use in a softmax classifier, according to \log_{10} population density using equal bin width over the range of population densities in LS. In Fig. 6 we show the LS population density range as sampled by MP-16 and the locations of the buckets. This results in four buckets of [‘lowest’, ‘low’, ‘medium’, ‘high’] density, with corresponding percentage of land area being [93.9, 4.93, 1.10, 0.029]%, respectively. Thus the LS classifier predicts these 4 classes. In Fig. 3 the medium population density bucket is overlain with the S^2 cells (fine) used for base (M, f^*) . The population density mask is more restrictive than the S^2 cells alone.

For LC, we use the top 22 top-level land cover classes to relabel the MP-16 images. We then merge these into 7

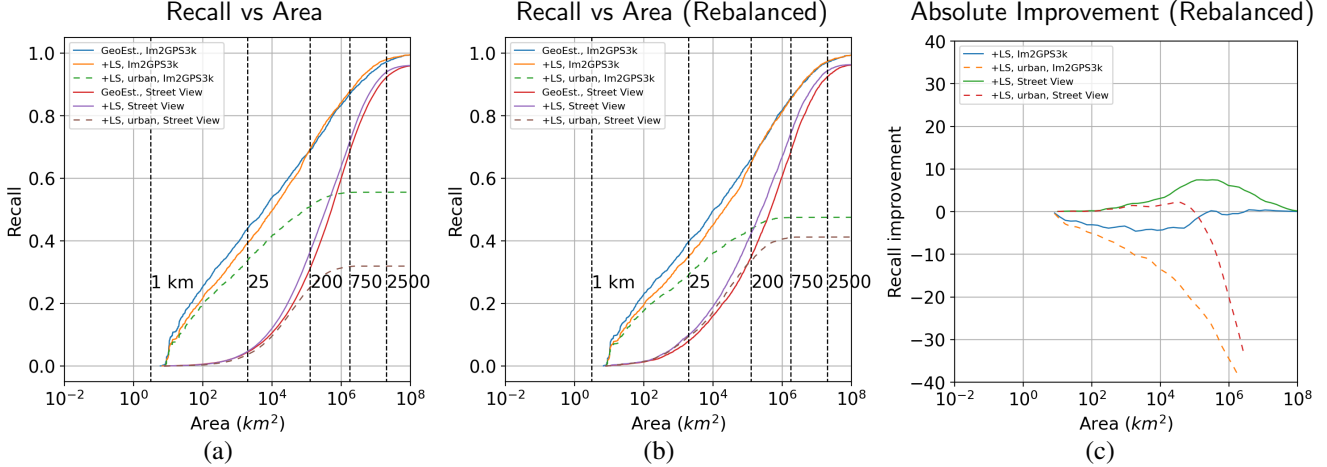


Figure 4. (a) *Recall vs. Area* obtained for rasterized GeoEst (Alg. 1), alone and ensembled with LandScan (+LS) attribute prediction. As an additional baseline, we compare to always applying the LS “urban” mask instead of predicting the bucket (+urban, dotted curve). Spherical cap areas shown in blacked dashed lines, see text for details. (b) RvA, measured on data rebalanced over urban and non-urban areas by randomly sampling equal number of images from each LandScan mask. Our method improves performance for less-populated areas while maintaining urban area results. (c) Relative improvement measured on the balanced datasets.

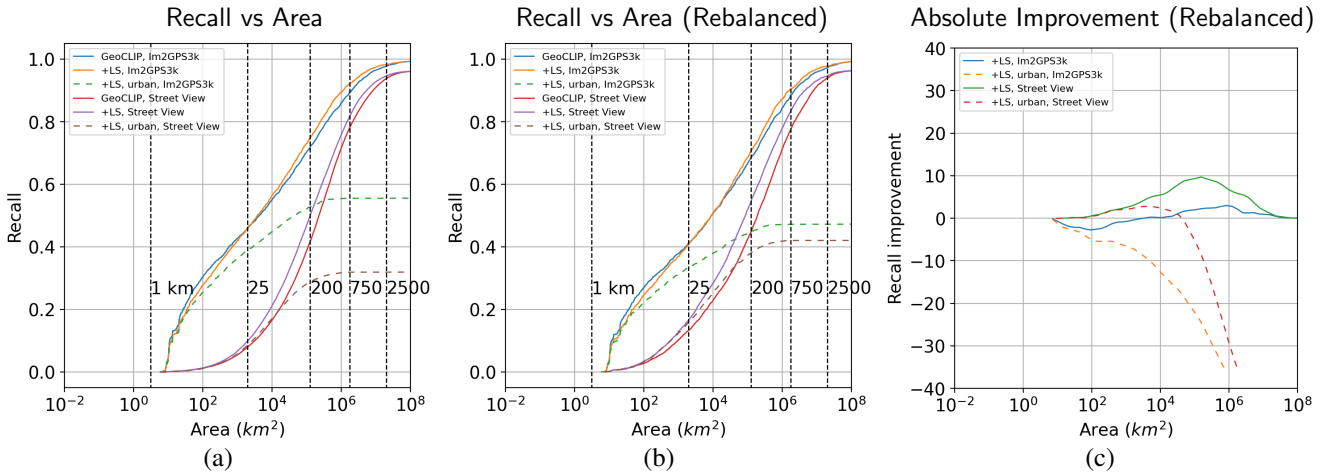


Figure 5. Rasterized GeoCLIP 1 and ensembling: same analysis as Fig. 4(a–c).

classes, that our LC classifier predicts (details in Sec. 5.2).

We manually balanced the classes in training by using only 12.5 % of the MP-16 images located in the ‘urban area’ LC category, since, by a large majority, the MP-16 images were located in densely populated areas, while our aim is to be able to locate both urban and rural locations.

For our predictors, we use a pretrained ResNet-50v2 architecture from [8], as implemented in the Pytorch Image Models (timm) [22]. Specifically we use the Big Transer (BIT)-M version of the model, which is trained on the public ImageNet21k dataset [15].

The predictors were trained on the relabeled MP-16 imagery for each of the LS classes for a maximum of 100 epochs using distributed training over 4 GPUs. In training,

the images were augmented using random cropping, rescaling, horizontal and vertical flipping, and color jitter.

5.2. Ensembling

In our experiments, the common image size was $H = 5400$ (latitude) by $W = 10800$ (longitude). This size was chosen as the dimensions are common factors to the the LS and LC TIFF image sizes, and was small enough to yield reasonable time complexity and geolocalization performance. Thus average resolution of the common image is ~ 4 km, which corresponds to zero recall at ~ 16 km² in Figs. 4 and 5, and Table 1.

For GeoEstimation, we used the hierarchical model (“base(M, f^*)” from [12]). For GeoCLIP, we used the

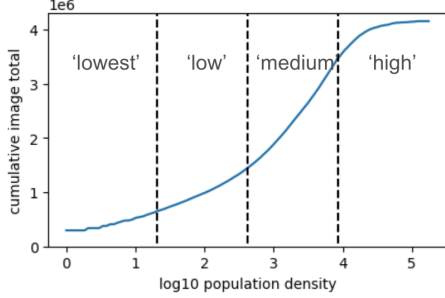


Figure 6. Cumulative distribution of MP-16 in LandScan (LS) population density. LS buckets shown as [‘lowest’, ‘low’, ‘medium’, ‘high’].

published model architecture and weights. Because both GeoEst. and GeoCLIP are fine-tuned with MP-16, we use the S^2 cell centers, which are also distributed according to MP-16, to sample the GeoCLIP location encoder and obtain scores for each of the S^2 cells.

To obtain $p \in \mathbb{R}^{M \times N}$, the S^2 cells from $\text{base}(M, f^*)$ were rasterized to the common image per Algo. 1. For a given image the rasterized probabilities of each pixel is obtained by summing the probabilities of all S^2 cell scores from GeoEst. or GeoCLIP intersecting that pixel.

The LS and LC TIFFs were downsampled by factor of 4 and 12 respectively, to the common image resolution. The binary masks in Algo. 2 were obtained from the downsampled images. Due to sparse sampling, some LC classes were merged by visual similarity prior to ensembling. All LS classes including cropland were merged (values 10-40 in [1]); all broad-leaf tree cover were merged (50–60); the remaining tree cover on dry land (70–100); short vegetation, incl. lichen and mosses (110–150); all vegetated and flooded regions (160–190); urban areas were not merged; and bare areas were merged with water and permanent snow and ice (200–220). Thus our models predict 7 classes for LC after merging.

5.3. Results

We evaluate the geolocation methods with Algo. 3 for both Im2GPS3k and the Street View dataset, based on panoids from [11]. Im2GPS3k and Street View both predominantly consist of urban areas with higher population density. To reduce this bias and better measure the effects on the rural and undersampled areas we are interested in, we rebalance the data by randomly sampling equal number of images from each LandScan mask bucket. The results are summarized in terms of Recall vs Area in Figs. 4 and 5 both with and without balancing, and Table 1 gives results for balanced imagery. We present results for baseline rasterized algorithm for GeoEst. or GeoCLIP predictions Algo. 1; ensembling per Algo. 2, with GeoEst. or GeoCLIP and LS

Method	Street 1 km	City 25 km	Region 200 km	Country 750 km	Continent 2500 km
GeoEst.	—	39.69	65.96	85.57	97.04
+LS	—	35.04	64.85	85.42	97.25
+LS, urban prior	—	29.01	43.78	47.45	47.50
+LC	—	36.74	65.64	86.32	97.10
+LS+LC	—	32.43	60.46	83.71	96.96

Im3GPS3k [19], GeoEst. and ensemble

Method	Street 1 km	City 25 km	Region 200 km	Country 750 km	Continent 2500 km
GeoCLIP	—	41.20	68.41	88.60	97.22
+LS	—	40.71	70.71	90.41	97.83
+LS, urban prior	—	33.53	44.92	47.22	47.22
+LC	—	40.30	71.39	90.13	97.68
+LS+LC	—	37.14	68.70	89.41	97.79

Im3GPS3k [19], GeoCLIP and ensemble

Method	Street 1 km	City 25 km	Region 200 km	Country 750 km	Continent 2500 km
GeoEst.	—	7.96	34.73	68.21	92.45
+LS	—	9.85	42.14	74.27	94.39
+LS, urban prior	—	9.36	33.63	41.06	41.21
+LC	—	8.29	40.25	75.43	94.37
+LS+LC	—	9.39	39.83	73.95	94.67

Street View [11], GeoEst. and ensemble

Method	Street 1 km	City 25 km	Region 200 km	Country 750 km	Continent 2500 km
GeoCLIP	—	13.28	44.70	77.51	93.97
+LS	—	16.56	54.42	83.37	94.62
+LS, urban prior	—	15.76	38.06	42.03	42.04
+LC	—	15.69	51.33	82.69	94.97
+LS+LC	—	16.09	53.25	83.21	95.03

Street View [11], GeoCLIP and ensemble

Table 1. Recall for rasterized GeoEstimation and GeoCLIP, Algo. 1 and ensembled attribute predictors, Algo. 2 for Im2GPS3k [19] and Street View data, based on [11] (Sec. 4.2). Recall is calculated as function of the area corresponding to a spherical cap with radius of the typical GCD thresholds ($3.1, 2.0 \times 10^3, 1.3 \times 10^5, 1.8 \times 10^6$, and $2.0 \times 10^7 \text{ km}^2$), see Fig. 4 (c)). Results shown for balanced data. The 1 km GCD threshold cap area is much less than the average area of the common image pixels, $\sim 16 \text{ km}^2$ (see Sec. 5.2), thus no results are available for this threshold.

(+LS); GeoEst. or GeoCLIP and LC (+LC); and GeoEst. or GeoCLIP with LS and LC (+LS+LC). We note that the resolution of our common image prevents us from locating images within the 1 km GCD threshold (see Sec. 5.2). Black dashed lines in the figures show the areas of spherical caps with radii corresponding to the GCD thresholds typically used in literature, e.g. [2, 12]. The recall of the remaining ensembles are summarized as a function of global spherical

cap areas. Since for our proposed approach, we are accumulating all proposed areas in our final probability map, per Eq. 1, we consider recall as a function of total area of these often discontinuous regions.

For Im2GPS3k, the image counts for each Land-Scan mask (from lowest to high population density) are [540, 548, 1159, 715]. To rebalance, we randomly sample 540 from each bucket to obtain 2160 images. Similarly, for Street View the images in each mask bucket were [11846, 17623, 18668, 1692], with the smallest number of images in the highest pop. density mask. Rebalancing results in 6768 images.

In Figs. 4, we see larger gains for Street View, and with the largest gains for all datasets in the larger area thresholds that generally correspond to rural areas. (Note there is also a drop in performance for both base models on the out-of-domain Street View dataset relative to the typical Im2GPS3k evaluation set; we are able to make up some portion of this difference). Figs. 4–5(c) show the absolute improvement in recall over the base models.

We also include an ‘urban prior’ model as an additional baseline, ‘+LS, urban’ which always applies a mask restricting to the two highest-density LS buckets. Since the original imagery is drawn primarily from urban regions, such a constant prior could also be effective. We find that the +LS attribute predictors outperform it, as expected, on larger area regions: the urban prior model discards these wholesale, while predicted population density improves performance for these areas. Thus the gains are not due simply to applying a mask for urban regions, and predicting different density attribute values is necessary to obtain improvements.

For the rebalanced datasets, there are reductions in recall overall for the Im2GPS3k set, and improvements for Street View. This is because the original Im2GPS3k dataset is biased toward the highest population density regions, and Street View samples the highest density mask considerably less. The recall on Im2GPS3k is reduced at smaller areas using our ensembling approach for the original and rebalanced datasets, with improvements at larger scales (see Fig. 4–5, Table 1), and peak improvements of 0.21 and 2.96 in absolute recall, for GeoEst and the SOTA GeoCLIP base models, respectively.

In Table 1, at smaller scales, e.g. spherical cap areas corresponding to 25 and 200 km, the +LS ensemble gave the largest improvements, with +LC and the full ensemble, +LS+LC, giving some benefits at larger scales.

The benefits of ensembling the ground-level attribute predictors at a global scale with a baseline ‘strong’ image geolocation predictor are apparent. The attribute predictors bring additional ground-truth information to the solution, and improve performance relative to baseline.

6. Conclusions and Future Work

We have introduced a new image geolocation metric, *Recall vs Area*, and an ensembling approach to global-scale image geolocation, which incorporates ground-level attribute predictors based on satellite data products. Our metric helps account for ground-level image similarity from different geographic regions, able to measure discontinuous predicted areas. Practical image geolocation systems are often concerned with search area, and Recall vs Area accounts for these needs naturally. By ensembling our ground-level attribute predictors, we have improved upon the SOTA method in image geolocation, GeoCLIP [2], in terms of RvA.

Our ensembling approach combines ground-level attribute predictors with geolocation models, to obtain improvements in image geolocation recall as a function of search area. The attribute predictors bring additional information to bear on the solution using satellite-based attribute masks, and improve performance relative to strong baselines, particularly in areas that are under-sampled in the original dataset.

Interestingly, the relative gain from ensembling predicted attribute masks was larger for GeoCLIP than GeoEst, even though it started at a higher performance level. The information in the embeddings could be complementary to our ground-level attributes. We will explore this in future work.

Satellite data has global coverage, and is not as constrained by geotagged information. By associating satellite-recognizable attributes to ground level images, we can extend information about location to areas of the world not included in any geotagged image data, since they are included in the satellite coverage. We validate this approach using population density and land use, but we hope to extend it to more general attributes, including those found implicitly through large datasets of image captions. More generally, automatically associating ground-level image features with mask areas recognizable by satellite promises to extend the geographic reach of these image features to undersampled regions.

References

- [1] European Space Agency. Esa: Land Cover CCI product user guide version 2.0, 2023. 1, 2, 4, 5, 7
- [2] Vicente Vivanco Cepeda, Gaurav Kumar Nayak, and Mubarak Shah. GeoCLIP: Clip-inspired alignment between locations and images for effective worldwide geolocalization. *arXiv preprint arXiv:2309.16020*, 2023. 1, 2, 3, 4, 5, 7, 8
- [3] Yi-Ting Chen, Jinghao Shi, Zelin Ye, Christoph Mertz, Deva Ramanan, and Shu Kong. Multimodal object detection via probabilistic ensembling. In *European Conference on Computer Vision*, pages 139–158. Springer, 2022. 4

- [4] Brandon Clark, Alec Kerrigan, Parth Parag Kulkarni, Vicente Vivanco Cepeda, and Mubarak Shah. Where we are and what we're looking at: Query based worldwide image geo-localization using hierarchies and scenes. *arXiv preprint arXiv:2303.04249*, 2023. 1, 2
- [5] Google. Streetview API, 2023. 5
- [6] James Hays and Alexei A Efros. Im2GPS: estimating geographic information from a single image. In *2008 IEEE conference on computer vision and pattern recognition*, pages 1–8. IEEE, 2008. 1
- [7] Sixing Hu, Mengdan Feng, Rang MH Nguyen, and Gim Hee Lee. CVM-Net: Cross-view matching network for image-based ground-to-aerial geo-localization. In *Proceedings of the IEEE Conference on Computer Vision and Pattern Recognition*, pages 7258–7267, 2018. 3
- [8] Alexander Kolesnikov, Lucas Beyer, Xiaohua Zhai, Joan Puigcerver, Jessica Yung, Sylvain Gelly, and Neil Houlsby. Big Transfer (BiT): General visual representation learning. In *Computer Vision—ECCV 2020: 16th European Conference, Glasgow, UK, August 23–28, 2020, Proceedings, Part V 16*, pages 491–507. Springer, 2020. 6
- [9] Martha Larson, Mohammad Soleymani, Guillaume Gravier, Bogdan Ionescu, and Gareth JF Jones. The benchmarking initiative for multimedia evaluation: MediaEval 2016. *IEEE MultiMedia*, 24(1):93–96, 2017. 1, 5
- [10] Tsung-Yi Lin, Serge Belongie, and James Hays. Cross-view image geolocation. In *Proceedings of the IEEE Conference on Computer Vision and Pattern Recognition*, pages 891–898, 2013. 3
- [11] Grace Luo, Giscard Biamby, Trevor Darrell, Daniel Fried, and Anna Rohrbach. G³: Geolocation via guidebook grounding. *arXiv preprint arXiv:2211.15521*, 2022. 1, 2, 3, 4, 5, 7
- [12] Eric Muller-Budack, Kader Pustu-Iren, and Ralph Ewerth. Geolocation estimation of photos using a hierarchical model and scene classification. In *Proceedings of the European conference on computer vision (ECCV)*, pages 563–579, 2018. 1, 2, 3, 4, 5, 6, 7
- [13] Shraman Pramanick, Ewa M Nowara, Joshua Gleason, Carlos D Castillo, and Rama Chellappa. Where in the world is this image? Transformer-based geo-localization in the wild. In *Computer Vision—ECCV 2022: 17th European Conference, Tel Aviv, Israel, October 23–27, 2022, Proceedings, Part XXXVIII*, pages 196–215. Springer, 2022. 2, 5
- [14] Alec Radford, Jong Wook Kim, Chris Hallacy, Aditya Ramesh, Gabriel Goh, Sandhini Agarwal, Girish Sastry, Amanda Askell, Pamela Mishkin, Jack Clark, et al. Learning transferable visual models from natural language supervision. In *International conference on machine learning*, pages 8748–8763. PMLR, 2021. 3
- [15] Tal Ridnik, Emanuel Ben-Baruch, Asaf Noy, and Lihl Zelnik-Manor. Imagenet-21k pretraining for the masses, 2021. 6
- [16] Paul Hongsuck Seo, Tobias Weyand, Jack Sim, and Bohyung Han. CPlaNet: Enhancing image geolocation by combinatorial partitioning of maps. In *Proceedings of the European Conference on Computer Vision (ECCV)*, pages 536–551, 2018. 2
- [17] K. Sims, A. Reith, E. Brigh, J. McKee, and A. Rose. Land-Scan Global 2021 [dataset]. 2022. 1, 2, 4, 5
- [18] Bart Thomee, David A Shamma, Gerald Friedland, Benjamin Elizalde, Karl Ni, Douglas Poland, Damian Borth, and Li-Jia Li. YFCC100M: The new data in multimedia research. *Communications of the ACM*, 59(2):64–73, 2016. 1, 4, 5
- [19] Nam Vo, Nathan Jacobs, and James Hays. Revisiting Im2GPS in the deep learning era. In *Proceedings of the IEEE international conference on computer vision*, pages 2621–2630, 2017. 1, 2, 4, 5, 7
- [20] Xiaolong Wang, Runsen Xu, Zhuofan Cui, Zeyu Wan, and Yu Zhang. Fine-grained cross-view geo-localization using a correlation-aware homography estimator. *Advances in Neural Information Processing Systems*, 36, 2024. 3
- [21] Tobias Weyand, Ilya Kostrikov, and James Philbin. Planet-photo geolocation with convolutional neural networks. In *Computer Vision—ECCV 2016: 14th European Conference, Amsterdam, The Netherlands, October 11–14, 2016, Proceedings, Part VIII 14*, pages 37–55. Springer, 2016. 1
- [22] Ross Wightman. Pytorch image models. <https://github.com/rwightman/pytorch-image-models>, 2019. 6